Ceramics International 49 (2023) 21561–21569

Contents lists available at ScienceDirect

Ceramics International

journal homepage: www.elsevier.com/locate/ceramint

Data-driven optimization of hardness and toughness of high-entropy nitride coatings

Shaoyu Wu [a], Xiaoqian Xu [a,d], Shani Yang [a], Jingwen Qiu [c], Alex A. Volinsky [e], Xiaolu Pang [a,b,*]

[a] *School of Materials Science and Engineering, University of Science and Technology Beijing, Beijing, 100083, China*
[b] *Beijing Advanced Innovation Center for Materials Genome Engineering, University of Science and Technology Beijing, Beijing, 100083, China*
[c] *School of Materials Science and Engineering, Hunan University of Science and Technology, Hunan, 411201, China*
[d] *Yangtze Memory Technologies Co, Ltd, China*
[e] *Department of Mechanical Engineering, University of South Florida, 4202 E. Fowler Ave. ENG 030, Tampa, 33620, USA*

ARTICLE INFO

Handling Editor: Dr P. Vincenzini

Keywords:
Machine learning
Multi-objective optimization
High-entropy
Coating
Toughness
Hardness

ABSTRACT

High coating hardness and toughness are mutually contradicting properties and are challenging to be achieved simultaneously. Combining the vast component space of high entropy systems and the powerful high-dimensional data processing tools is expected to be the best solution to this problem. In this paper, high-entropy nitride coatings data for quinary and hexagonal systems were collected and machine learning prediction models were trained. Using a new material system combined with multi-objective optimization, high-entropy nitride coatings with the optimal hardness and elastic modulus combination were successfully obtained and verified by experiments. In addition, the partial dependence heatmaps were used to visualize how elemental content affects mechanical properties prediction in this system. This approach helped to better interpret the optimization results and discover the unknown mapping relationships between elemental content and the mechanical properties of high-entropy nitrides in machine learning models.

1. Introduction

Hard coatings are often used to improve the substrate's durability, strength, and wear resistance. The common hard coatings include titanium nitride [1], chromium nitride [2], and tungsten carbide [3]. These materials are typically used in automotive, aerospace, and medical [4] applications. However, hard coatings' drawback is their poor toughness [5], making them more susceptible to cracking or chipping when exposed to extreme temperatures or stresses. Hence, there is a pursuit for hard coatings with combined high hardness and toughness, which are contradicting properties. Generally, hardness measures a material's resistance to plastic deformation and wear, while toughness measures the resistance to crack propagation. Thus, hard materials are less likely to plastically deform and in turn, have poor toughness. Many methods have been tried to solve this problem, including doping elements [6]. However, current elemental doping is limited to binary or ternary systems, with mediocre results.

High-entropy materials are alloys or compounds composed of five or more elements in roughly equal proportions [7]. These materials have a high degree of disorder or randomness, resulting in a higher degree of entropy. High-entropy materials have exhibited a number of desirable properties, such as increased strength, improved corrosion resistance, and better wear resistance [8–10]. Also, high-entropy materials have shown good performance and a combination of contradictory properties, like Cantor alloy. The Cantor alloy has high yield strength and extremely high fracture toughness at a low temperature of 77 K [10]. It is expected that high-entropy materials can achieve optimized hardness and toughness. However, since these materials are composed of multiple elements and have a wide range of configurations, their properties can be difficult to predict. Therefore, methods able to efficiently and scientifically process high-dimension and massive amounts of information are needed.

Data-driven research methods represented by machine learning have become a hot topic in the field of materials science and engineering. Machine learning is a powerful tool for materials science, as it can be used to analyze large datasets and identify patterns and correlations that may not be obvious. Machine learning can also be used to predict and develop new materials with desired properties, such as strength, durability, and electrical conductivity. Zhang et al. [11] proposed a machine learning strategy that significantly improves the ultimate tensile

---

[*] Corresponding author. School of Materials Science and Engineering, University of Science and Technology Beijing, Beijing, 100083, China.
E-mail address: pangxl@mater.ustb.edu.cn (X. Pang).

https://doi.org/10.1016/j.ceramint.2023.03.292
Received 4 March 2023; Received in revised form 24 March 2023; Accepted 29 March 2023

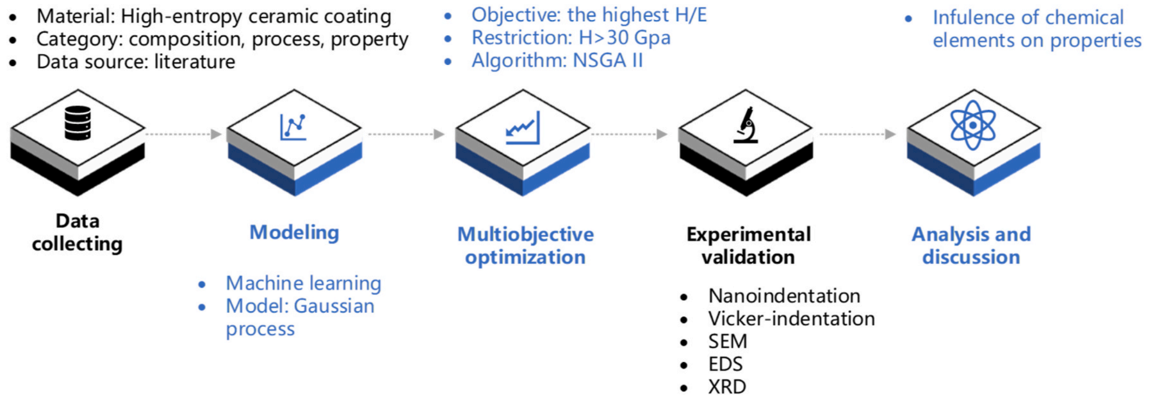

Fig. 1. Workflow diagram of data-driven analysis for multi-objective optimization of HEN coatings.

(2) Machine learning models

strength (UTS) and electrical conductivity (EC) of alloys, by identifying a set of key features through relevance screening, recursive elimination, and exhaustive screening of datasets. He et al. [12] proposed a machine learning strategy, which can accurately predict the phase diagrams of multi-component ferroelectric systems $(Ba_{1-x-y}Ca_xSr_y)(Ti_{1-u-v-w}Zr_uSn_vHf_w)O_3$ by combining classification and regression methods. Using a Crystal Graph Convolutional Neural Networks model, Hou and Wang et al. designed potential MAX phases with enhanced and tunable mechanical properties based on their crystal structure [13]. They also developed a novel approach that integrates a real physical picture model with an independent screening and sparsification operator method, leveraging machine learning algorithms to understand the complex oxidation of various ceramics and alloys [14]. Moreover, they applied a back propagation artificial neural network to investigate the multi-stage oxidation of Al_4SiC_4, accounting for the effects of temperature, time and aspect ratio [15]. However, it's hard to achieve accurate and simultaneous prediction of multiple objective properties by directly using machine learning because the models may not be able to accurately capture the trade-offs between different objectives, leading to inaccurate predictions.

A multi-objective optimization is a useful tool for finding the best trade-off between different objectives that have conflicting requirements. It can be used to identify solutions that are optimal for all objectives, or to find a compromise between objectives, helping to make decisions in a wide range of applications. Li et al. [16] successfully prepared several new high-entropy alloys with good hardness and saturated magnetization by using genetic algorithms. Khatamsaz et al. [17] used Bayesian optimization to optimize Pugh's ratio and Cauchy pressure of the MoNbTiVW alloys and obtained refractory multi-principal-element alloys with excellent ductility. Therefore, multi-objective optimization is promising for predicting materials with desired hardness and toughness.

Although data-driven approaches, represented by machine learning, have shown surprising performance, the black-box nature of these methods hinders people from understanding the underlying mapping relationships, and mistrust of the results impedes the participation and guidance of more professionals in various fields. Therefore, efforts to enhance the interpretability of machine learning have received increasing attention to improve the credibility of results [18,19]. In addition, interpreting the results of well-performing machine learning models can uncover hidden important relationships and guide materials research. Iwasaki et al. [20] extracted surprising new knowledge from interpretable machine learning and synthesized a new type of spin-driven thermoelectric material with the largest thermoelectric power to date. Fang et al. [21] discovered possible physical phenomena that may affect key performance by interpreting the convolutional neural network predictions of the UTS of nickel-based alloys. Therefore, exploring the unknown mapping relationship between features and prediction through the interpretability of machine learning is of significant importance.

This work aims to obtain high-entropy nitride (HEN) coatings with high hardness and toughness through data-driven research methods and explore the relationships between elements and properties in machine learning models. In the study of coating materials, the high ratio of hardness (H) to Young's modulus (E) often serves as a performance indicator. Brittle materials with a high H/E ratio can tolerate more deformation, indicating good toughness [22]. Thus, in this work, the machine learning models will be established around H and E. Models will also be used for the multi-objective optimization to find hexagonal element HEN coatings with high H and low E, and actual mechanical properties will be verified by experiments. To enhance the mechanical properties of the coating, a hexagonal HEN with high elemental diversity was chosen based on Gibbs function, aiming to achieve a high configurational entropy and a stable single-phase solid solution, and thus to maximize the benefits of high entropy effect. In addition to optimizing the mechanical properties of the HEN coatings, the elements affecting the multi-objective optimization and their varying contents' effects on H and E will be shown through partial dependence heatmaps. This work demonstrates an efficient way to interpret optimized results from the algorithm's perspective and discover the potential effects on mechanical properties in new HEN systems.

2. Materials and methods

(1) Design strategy

The workflow diagram of the overall process used in this work is presented in Fig. 1. First, the content of the database is determined, including the composition and properties of HEN coatings, and the database is filled with data collected from the literature. Based on the data distribution in the database, the search space is determined, and then reliable properties prediction models are established through machine learning. The non-dominated sorting genetic algorithm II (NSGA-II) multi-objective optimization is used to find the optimal composition with high H and low E in the search space. After the optimal composition is verified through a series of characterization, the partial dependence heatmaps are plotted to show how elements affect H and E through variations in content.

The composition and process parameters are used in this work, including the deposition temperature, target power, and bias voltage of various coatings as input variables in the dataset, along with the corresponding H or E as output variables to train a regression model for predicting the properties of HEN coatings. 20% of the dataset will be split into a test set, and the rest will be used for training. Among the five

Table 1
Composition range in at.% and hardness in the hardness dataset.

	Elemental content (at.%)														Hardness (GPa)
	N	Al	Cr	Si	Ti	V	Zr	Nb	Mo	Ta	Hf	Y	Mn	Ni	
min	11.8	0	0	0	0	0	0	0	0	0	0	0	0	0	8.6
Max	65.3	18.8	29.6	16.6	18.7	16.8	19.1	13.1	14.9	18.9	13.6	13.7	7.3	9.1	41.1

common regression models, we select the one with the best performance through 10-fold cross-validation using the root mean square error (RMSE) as the evaluation metric [6]. The purpose of the 10-fold cross-validation is to assess the presence of overfitting. The hyperparameter optimization of the models uses Bayesian optimization, with the sampling function selecting the expected improvement over 40 iterations. The optimization effect is evaluated using the regression metrics of 10-fold cross-validation, including RMSE, mean absolute percent error (MAPE) [16], and determinant coefficients (R^2) [6]. In addition, the same metrics are used to evaluate the actual prediction effects of the models on the test set.

(3) Search space

The search space which includes the varying content of six alloying elements and N element is defined based on statistical results from the dataset and the definition of high entropy. According to the research of Yeh et al. [23], the content of alloying elements in high-entropy systems is 5–35 at.%. Therefore, the search space for each element is the intersection of the range of the dataset and the definition of high entropy.

(4) Multi-objective optimization

Multi-objective optimization is implemented using the optimization toolbox in MatLab. Before starting multi-objective optimization, the problem needs to be defined, including the number of variables and their search space, the optimization objectives and corresponding objective functions, and any constraints. In this work, the variables and search space have already been determined as $x = [x_1, x_2, x_3, x_4, x_5, x_6, x_7] = [c_N, c_{Al}, c_{Cr}, c_{Si}, c_{Ti}, c_{Mo}, c_{Ta}]$, where c represents the elemental content, and the optimization objectives have been determined as maximizing H and minimizing E to achieve the optimal H/E values. However, in multi-objective optimization, the optimization direction of H and E is the same, so the objective value H is reversed to a negative number and both H and E are minimized to achieve the desired result. The objective functions $f_1(x)$ and $f_2(x)$ are the machine learning prediction models for H and E, respectively. The constraints include the sum of the elemental contents being equal to 100% and the target H value greater than 30 GPa. Therefore, the multi-objective optimization problem can be represented as:

$$\begin{aligned} & \mathit{Minimize}\ F(x) = [-f_1(x), f_2(x)] \\ & \quad \mathit{subject\ to}\ 30 - f_1(x) < 0 \\ & \sum x_i = 100, i = 1, 2, \dots, 7 \\ & \qquad x_1 \in [12, 65] \\ & \qquad x_2 \in [5, 19] \\ & \qquad x_3 \in [5, 20] \\ & \qquad x_4 \in [5, 17] \\ & \qquad x_5 \in [5, 19] \\ & \qquad x_6 \in [5, 15] \\ & \qquad x_7 \in [5, 19] \end{aligned} \tag{1}$$

For solving the multi-objective optimization problem, we need to choose an algorithm and set the corresponding parameters. In this work, the genetic algorithm NSGA-II was selected. NSGA-II is a common multi-objective optimization algorithm with the advantages of less computation time and a high probability of obtaining good results. The initial population size was set to 500 and the maximum evolutional generation was set to 2,000 for NSGA-II, while other parameters were set to the default values in the algorithm template. Finally, the appropriate solution was selected from the Pareto front obtained from the solution based on the size of H/E and H, and then samples were prepared for experimental verification.

(5) Partial dependence analysis

Partial dependence represents the relationships between predictor variables and predicted responses in a trained regression model [24]. It is used to show how a subset of variables affects the result of a function by marginalizing the other variables. It can be used in machine learning models to show how features influence model predictions. Specifically, the partial dependence analysis can provide a single effect of one feature, or a mutual dependence between two features. Moreover, this work emphasizes the mean effect of the entire model across all data points, instead of the predictions for single data points or subpopulations, which helps to uncover the general pattern and rule of how element content influences property prediction. Thus, based on the experimental validation of the feasibility of machine learning and multi-objective optimization, we generated partial dependence heatmaps for specific element combinations using the machine learning model and the dataset. These heatmaps display the effects of element content on mechanical properties predictions, provide the mapping relationship between them, and explain how the optimal element content is determined in the Pareto front, thereby enhancing the interpretability and credibility of the multi-objective optimization results. Since the partial dependence heatmaps are statistically supported by a large number of experimental data from the literature, they can also deepen the understanding of the role of alloying elements in the HEN system.

(6) Experimental procedure

In this work, coatings were prepared using high-throughput magnetron sputtering. The coatings were deposited on 10 mm diameter Si (100) substrates (0.4 mm thick) using a JCP 500 magnetron sputtering system equipped with three targets. The targets were AlTi (1:1), CrMoTa (1:1:1), and Si, with a purity of 99.9%. The power of the three targets was 80 W, 100 W, and 50 W, respectively. The remaining deposition parameters can be found in Ref. [6]. To control the composition of the coatings, high-throughput preparation was used, which involved placing 16 silicon wafers on a stationary sample stage at the same time. Composition gradients were formed by different positions of the wafers and the target power, and the coating samples with the closest expected composition were selected. The coatings' thickness, surface morphology, and microstructure were obtained using a scanning electron microscope (SEM). The coatings' quantitative composition evaluation was obtained using energy dispersive spectroscopy (EDS) in an SEM. The coatings' phase structure was determined using X-ray diffraction (XRD). The coatings' hardness and modulus were obtained using a nanoindenter. The EM1500L Vickers hardness tester was used to qualitatively characterize the coatings' toughness.

Table 2
Composition range in at.% and elastic modulus in modulus dataset.

	Elemental content (at.%)														Modulus (GPa)
	N	Al	Cr	Si	Ti	V	Zr	Nb	Mo	Ta	Hf	Y	Mn	Ni	
min	11.8	0	5.4	0	0	0	0	0	0	0	0	0	0	0	146.2
Max	65.3	18.8	19.9	16.6	18.7	16.8	19.1	7.3	14.9	18.9	13.6	13.7	7.3	9.1	435.9

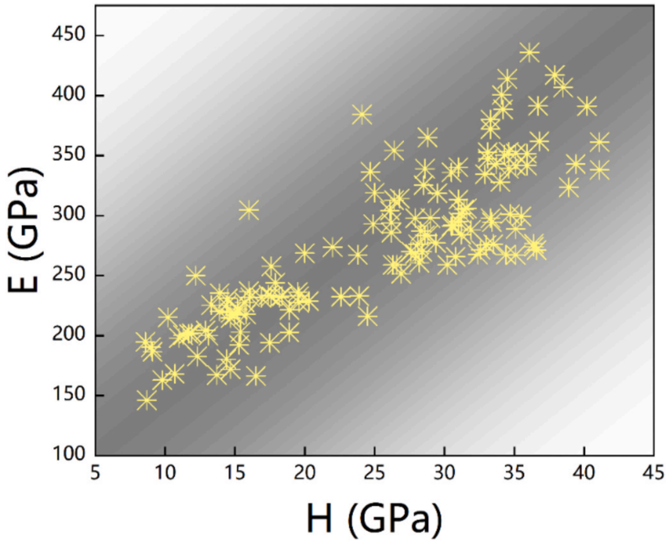

Fig. 2. The distribution of H and E in the dataset of HEN coatings.

3. Results and discussion

3.1. Data collection and search space

In this work, approximately 300 sets of data were obtained from the literature. The range of the two datasets is listed in Tables 1 and 2, with 167 sets of data for H and 134 sets of data for E, covering quinary and hexagonal element HEN coatings. To remove the effects of coating fabrication method, substrate material and coating morphology on mechanical properties, data from HEN coatings prepared by magnetron sputtering were selected. In addition to the composition of the coatings, the data also include process parameters such as deposition temperature, target power, and bias voltage, which are important factors for mechanical property. Pierson correlation analysis was performed using composition and process parameters as input variables and property as the output variable, and a low correlation was found, which is beneficial for obtaining a prediction model with good generalization. See Ref. [6] for specific details. In addition, the H and E of the same HEN coatings in the dataset were statistically analyzed, and the results are shown in Fig. 2, finding that H and E are correlated. If machine learning is used to predict H and E simultaneously, this correlation may be ignored, resulting in a prediction accuracy decrease. Therefore, multi-objective optimization is needed to predict the composition while considering the correlation between H and E.

As for determining the material system needed to be prepared and the corresponding search space, there are only 44 sets of hexagonal alloy-element systems in the dataset, which include (AlCrTiZrMoTa)N, (AlCrSiTiVNb)N, (AlCrSiTiZrTa)N, (AlCrZrMoMnNi)N and (AlCrSiTiZrMo)N. Facing the vast search space of hexagonal HEN composition, the Al, Cr, and Ti elements common to all systems are selected by considering the generalization ability of machine learning. Research has shown that adding an appropriate amount of Si can optimize the mechanical properties of coatings by refining the grains and changing the microstructure [25]. When the content of Si is low, the Si atoms may dissolve in the solid solution structure with a smaller atomic diameter, causing a solid solution strengthening. Thus, the coating's hardness has improved through solid solution strengthening and grain refinement. In addition, the coating crystallinity decreases with Si content, inducing a nanocomposite structure by forming an interfacial Si_3N_4 phase between crystal phases [26]. The interaction between amorphous and crystalline phases has improved the hardness of the coating [27]. However, a further increase in Si content will decrease the amount of columnar crystals and subside grain boundaries, presenting a dense glassy structure, in turn, weakening the mechanical properties of the coating [28]. As for the Mo element, it can easily react with the N element to form MoN, which has a high hardness, high melting temperature, and good thermal stability. Mo can also improve the friction resistance of the coating by forming MoO_3 to reduce friction and wear. According to the role of the above elements, a new HEN system (AlCrSiTiMoTa)N was selected for subsequent multi-objective optimization.

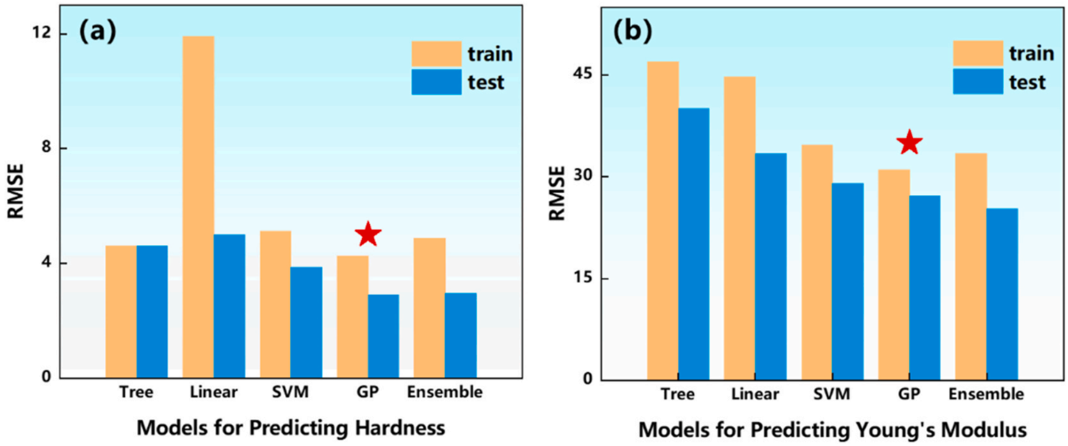

Fig. 3. Evaluating machine learning models using 10-fold cross-validated RMSE: (a) train error and test error for predicting hardness; (b) train error and test error for predicting Young's modulus.

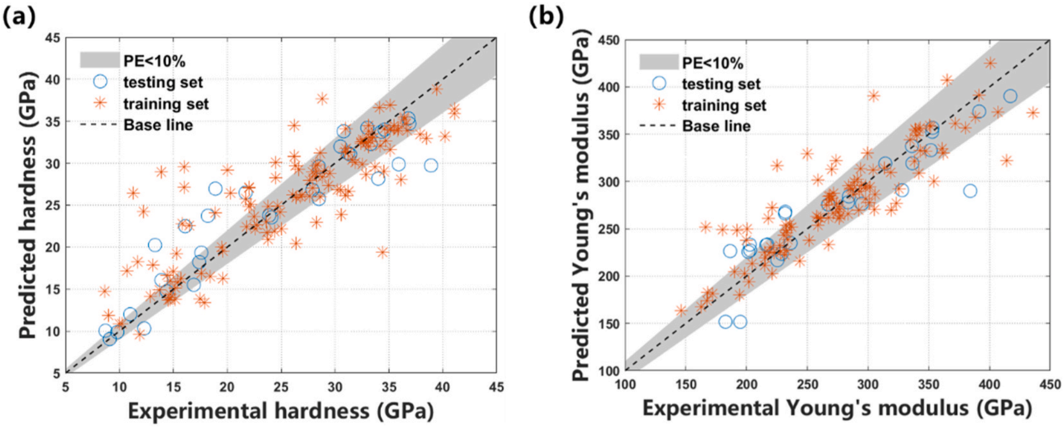

Fig. 4. The predictive performance of trained GP models: (a) hardness via GP; (b) Young's modulus via GP.

Table 3

Regression metrics of trained models.

Models	R^2		RMSE		MAPE	
	Training set	Testing set	Training set	Testing set	Training set	Testing set
H	0.67	0.82	4 GPa	3.5 GPa	13.6%	11.6%
E	0.74	0.78	27.8 GPa	28.6 GPa	7.4%	8.3%

3.2. Machine learning and multi-objective optimization

In order to obtain machine learning (ML) models with good prediction performance, the best one was selected from the common machine learning regression models, such as tree, linear, support vector machine (SVM), Gaussian process (GP), and ensemble models, by using a 10-fold cross-validated RMSE metric, and the results are shown in Fig. 3. Overall, the GP model has the lowest RMSE for hardness and Young's modulus predictions (although the RMSE of the GP model of the test set is slightly higher than the ensemble model for Young's modulus prediction), so subsequent model training and optimization is carried out with the GP model.

After Bayesian optimization of the hyperparameters including kernel function, kernel scale, and sigma of the GP model with the sampling function as the expected improvement, the response plots of the predicted values to the actual values for the H and the E prediction models are shown in Fig. 4. The R^2, RMSE and MAPE results for the 10-fold cross-validation as well as the test set are listed in Table 3. As shown in Table 3, after ten-fold cross-validations, the H model and the E model have R^2 values of 0.67 and 0.74 on the training set, respectively. On the test set, their R^2 values are 0.82 and 0.78, respectively, which are higher than those on the training set, indicating no overfitting issue. Table 3 also shows that the E model has a good regression metric, with a 10-fold cross-validation R^2 close to 0.75 and a percentage error within 10%. In contrast, the regression metric of the H model has a relatively normal performance, indicating that more high-quality data are needed to improve the predictive performance of the H model. However, Fig. 4(a) shows that the predicted data points for both the training and test sets are mainly discrete below 30 GPa, and the predicted values are somewhat excessive. In contrast, the predicted data points above 30 GPa mostly converge to the baseline, with the other discrete data points exhibiting values lower than the experimental. Furthermore, the distribution of data points in the PE region is similar to the E model, and presumably, the regression metric here is also close to the E model. Thus, the H model has a good high hardness prediction capability, which is favorable to the subsequent multi-objective optimization. As illustrated in Fig. 4(b), the distribution of discrete data points for the E model follows a similar path to the H model, i.e., data points below 300 GPa have excessive values, and data points above 300 GPa have lower values. However, most of the data points are concentrated within the PE region, indicating that the E model has good predictive performance and can support subsequent multi-objective optimization.

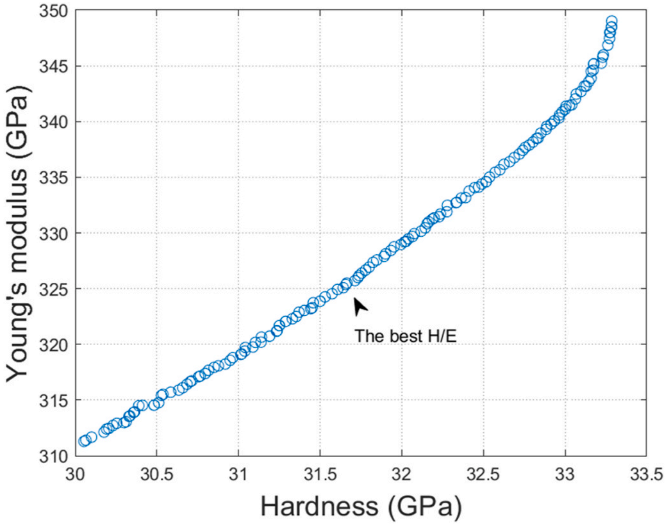

Fig. 5. Pareto front of H and E in search space.

Table 4

The optimized composition selected for experimental validation.

Elemental content (at.%)							Property (GPa)	
N	Al	Cr	Si	Ti	Mo	Ta	H	E
54	10	10	5	9	5	7	31.7	325

Through multi-objective optimization, a continuous and complete Pareto front that is shaped to protrude towards high H and low E is obtained, shown in Fig. 5. Based on the Pareto front points with lower tangent slopes and high H values, we selected the optimal solution, which is marked by the arrow in Fig. 5, and the optimal composition and corresponding H and E are listed in Table 4.

3.3. Experimental validation

To verify the optimal solution obtained through multi-objective optimization, the HEN coatings are characterized in terms of composition, morphology, structure, and mechanical properties. Fig. 6(a) shows

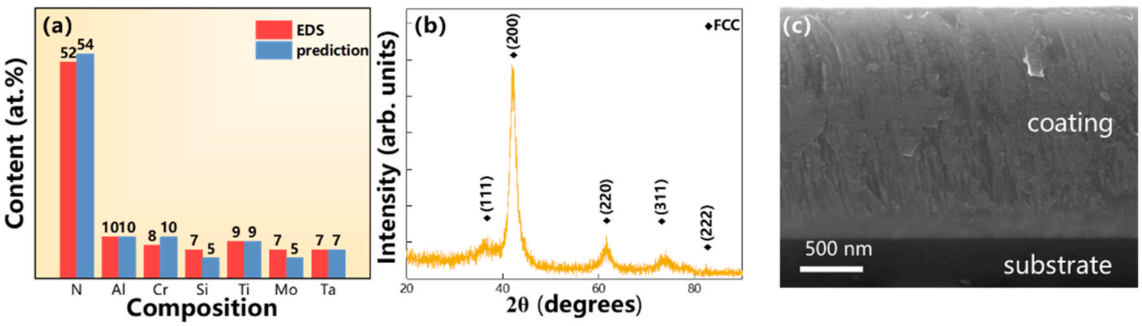

Fig. 6. Composition and microstructure of HEN coating: (a) comparison of the composition detected by SEM-EDS and predicted by NSGA-II; (b) XRD pattern; (c) SEM image of the cross-section.

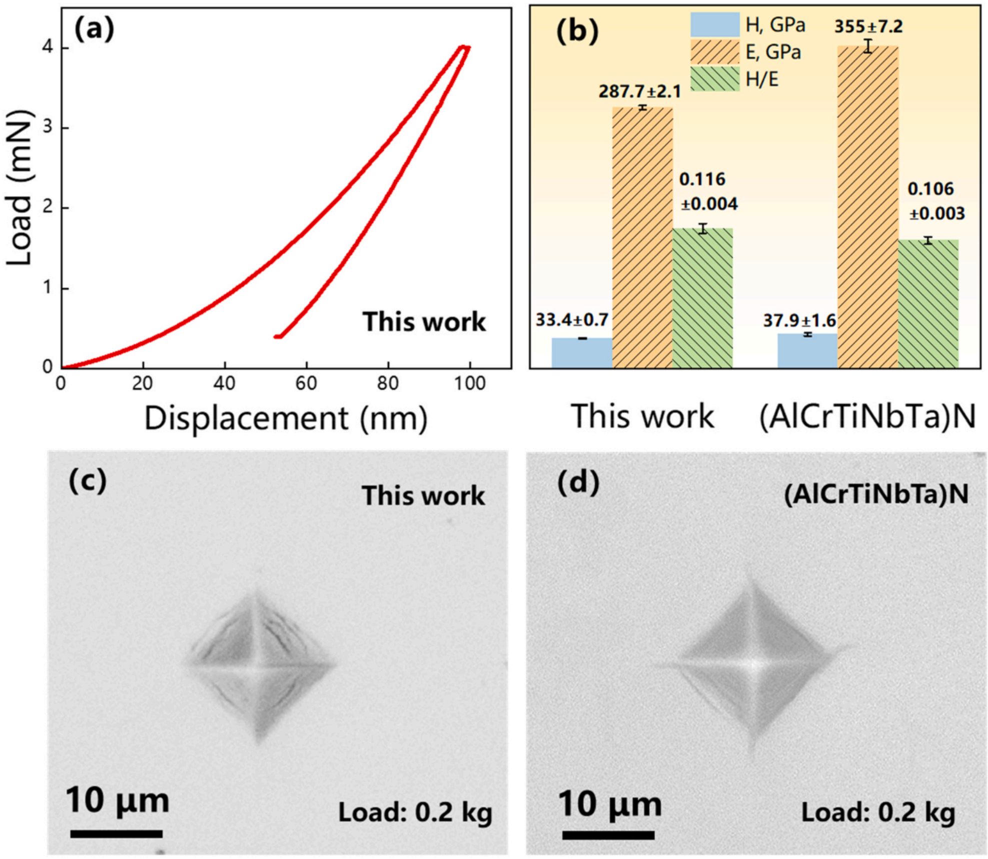

Fig. 7. Comparing hardness and toughness of HEN coatings made in this work (AlCrSiTiMoTa)N and previous work (AlCrTiNbTa)N: (a) load-displacement curves of this work obtained by nanoindentation; (b) H, E, and H/E of this work and (AlCrTiNbTa)N; (c) Vicker indentation of this work with 0.2 kg load; (d) Vicker indentation of (AlCrTiNbTa)N with 0.2 kg load.

that the nitrogen content of the HEN coating samples is around 50 at.%, and the distribution of the Al, Cr, Si, Mo, Ta, and Ti elements is relatively uniform, in accordance with the optimal composition obtained by the NSGA-II in Table 4. There is about a 2 at.% difference in the content of the N, Cr, Si, and Mo elements, which can be attributed to differences in the composition of the target material or differences in the sputtering yields of the elements, which are acceptable errors. The structure is shown in Fig. 6(b), and the coating still forms a single FCC solid solution phase structure, maintaining the characteristics of the high-entropy system. Fig. 6(c) shows the cross-sectional morphology of the coating, which is a columnar crystal structure with no obvious defects and a measured thickness of around 1.7 μm. Although the Si element tends to cause the coating to have an amorphous structure, the combination of the XRD spectra and SEM cross-sectional image can show that a 7 at.% Si content is appropriate and still allows the coating to maintain a single-phase solid solution structure of a high-entropy material.

The results of nanoindentation and Vickers indentation of the HEN coating are shown in Fig. 7, where Fig. 7(a) and (b) give the results of nanoindentation and Fig. 7(c) and (d) give the results of Vickers indentation. In the nanoindentation test, we used a maximum load of 4 mN, a loading time of 15 s, a peak dwell time of 10 s, and a total time of about 110 s. For this sample, we performed indentation at five different locations and averaged the outcomes to get the final measurement result. For Vickers indentation, we applied a load of 0.2 kg at three different locations each time. In this work, toughness was qualitatively evaluated by observing radial crack length produced in Vickers indentation. In addition, to further evaluate the toughness of the HEN coating prepared in this work, the nanoindentation results and Vickers

Table 5
Range of elemental content in at.% at each point in the Pareto front.

	N	Al	Cr	Si	Ti	Mo	Ta
min	54	10	5.9	5	7.4	5	5.2
max	56.4	14.4	10.3	5.6	9.5	5.4	6.8

indentation results of the quinary element HEN coating (AlCrTiNbTa)N prepared in our previous work [6] under the same conditions were compared. The nanoindentation data are referenced from it, and the Vickers indentation was completed in this work. First, the hardness of the HEN coating in this work was evaluated. Based on the Oliver-Pharr hardness calculations [29], the average values of H and E for the coating were obtained from the load-displacement curves in Fig. 7(a) and shown in Fig. 7(b). The hardness of the HEN coating in this work is greater than 30 GPa, which has reached the standard for hard coatings, although the value is lower than (AlCrTiNbTa)N. For the toughness of the HEN coating in this work, its E is much lower than the (AlCrTiNbTa)N coating, resulting in a higher H/E ratio of 0.116, which suggests a better toughness. Comparing the Vickers indentation at 0.2 kg load, the (AlCrTiNbTa)N coating had obvious radial cracks in Fig. 7(d), while no radial cracks exist in the coating made in this work in Fig. 7(c). The sample in this work underwent more deformation before fracture, further proving a better toughness.

In addition, by comparing the results in Table 4 and Fig. 7(b), the measured hardness is higher than the predicted result of NSGA-II, with an error of approximately 6.6%, while the measured modulus is lower than the predicted result, with an error of approximately 11.5%. As mentioned earlier, the H and E models have the problem of predicting high hardness to be low and predicting low modulus to be high. Thus, in future work, more data with high hardness and low modulus will be added to improve the accuracy of the prediction model and multi-objective optimization.

3.4. Partial dependence analysis

Based on the above process, a new HEN coating with high hardness and toughness was successfully prepared, verifying the feasibility of the machine learning model and multi-objective optimization. In this section, partial dependence heatmaps will be given to analyze the effects of element content on mechanical properties, summarize the relationships between them, and explain how the optimization results were determined.

Table 5 lists the maximum and minimum values of elemental content in the optimal solution given by multi-objective optimization, which shows that the NSGA-II algorithm has fully learned the rule that a coating with a sufficient amount of N can achieve higher hardness. In addition, the variance in the content of Al and Cr elements is the highest, indicating that they are the most critical elements that affect the choice between hardness and modulus. Thus, partial dependence heatmaps of Al and Cr on H and E in the machine learning model are plotted in Fig. 8 (a) and (b), despite the partial dependence heatmaps showing H and E values lower than 30 GPa and 300 GPa, respectively. This is due to the data processing used to generate the maps ignoring the participation of other features, leading to the lower values of H and E, rather than being an inaccurate prediction by the machine learning model.

Based on Fig. 8(a), the bright-colored squares are mainly concentrated along the lower edge of the image, suggesting that a lower Cr content (between 5 at.% and 10 at.%) can increase hardness. The colored squares mainly vary along the vertical axis, with a maximum difference of 6 GPa for H. In contrast, they remain relatively uniform and consistent within a larger range along the horizontal axis, indicating that H is less sensitive to changes in Al content, while Cr is the main factor affecting hardness. Fig. 8(b) shows that the peak value of E appears in

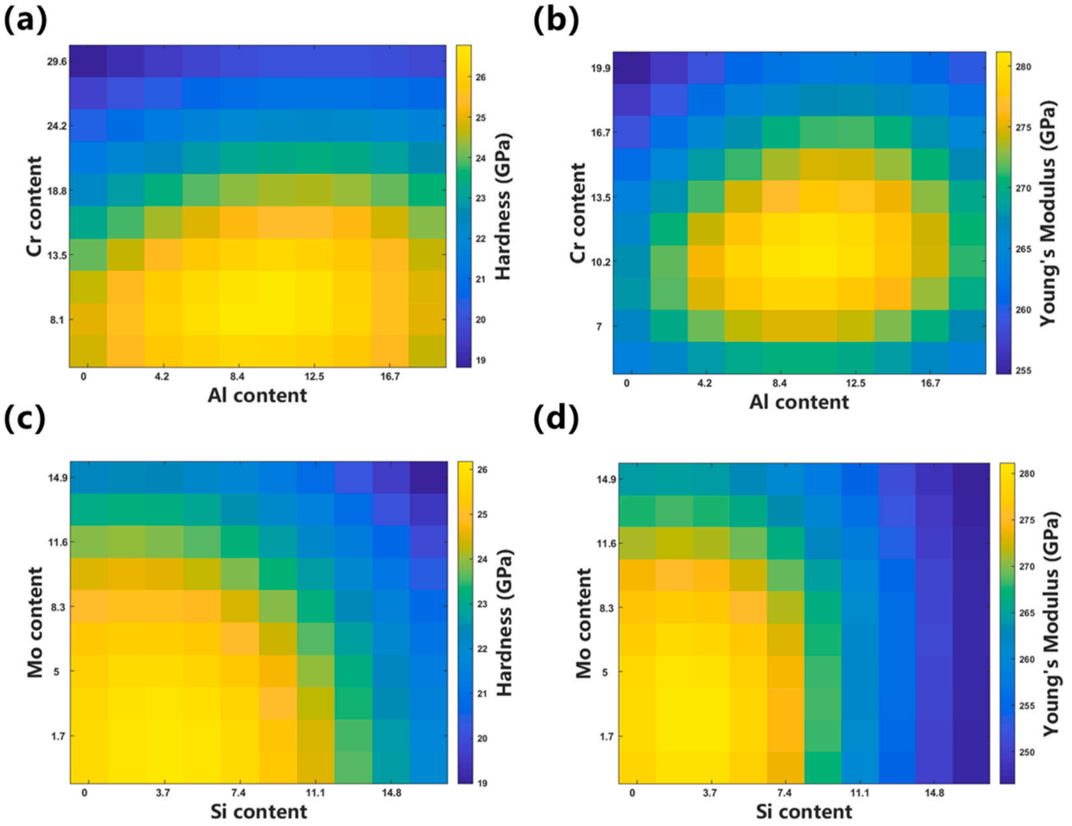

Fig. 8. Influence of dual elemental variables on predicted H and E from ML models, shown by partial dependence heatmaps: (a) Al and Cr upon E; (b) Al and Cr upon H; (c) Si and Mo upon E; (d) Si and Mo upon H.

the center of the image, indicating synergistic effects of Cr and Al on modulus enhancement, requiring both Cr and Al to reach certain content levels (10 at.% for Cr, from 8 at.% to 10 at.% for Al). The mapping relationship shows that Cr content between 8 at.% and 10 at.% achieves high hardness, whereas Al has less effect on H. Both Cr and Al exhibit similar behavior in affecting E, showing a trend of first increasing and then decreasing as their content increases. When their content is fixed at a close level, E can be significantly enhanced. Therefore, for NSGA-II to optimize the results, a lower Cr content (between 5 at.% and 10 at.%) should be first determined to obtain higher hardness. To gain lower E, the Al content needs to be adjusted to achieve the optimal content similar to Cr. Thus, the optimal content of the Al element is in a relatively high range (between 10 at.% and 15 at.%), considering that the content of Cr has been determined to be relatively low. This explains the distribution of optimal Al and Cr content with the best H/E ratio in the Pareto front.

Since Si and Mo are new elements introduced into this system, in order to investigate their mutual influence, partial dependence heatmaps were plotted. Fig. 8(c) shows that the peak of H gradually decreases along the diagonal toward the upper-right corner of the image. This indicates that the addition of a small amount of Si and Mo can enhance H, but the increasing content will weaken it. The diagonal symmetry shown in Fig. 8(c) suggests that the effects of Si and Mo on H are similar in magnitude and trend. Similarly, a small amount of Si and Mo can strengthen E. However, compared to Fig. 8(c), the bright-colored region in Fig. 8(d) contracting along the horizontal axis indicates that E is more sensitive to Si content. Additionally, when Si reaches its maximum, the regions on the image become indistinguishable, indicating that E is no longer affected by Mo, which is still undiscovered for the HEN. Therefore, the interpretation of the optimization results is that, given the problem definition, the NSGA-II needs to prioritize the component with the highest H. However, due to the definition of high entropy used in this work, the search space for all element contents has been set to greater than 5 at.%. The optimal content for Si is determined to be between 5 at.% and 5.6 at.%, while the optimal content for Mo is 5 at.%. To achieve the lowest E, it is necessary to increase the content as much as possible, but the available range is limited, resulting in the optimal Si and Mo content for H/E being around 5 at.%.

The above analysis revealed the potential mapping relationships between elements and performance. However, these relationships are based on the simplified and averaged feature influence by partial dependence, which fails to capture the heterogeneity or variation at individual or group level. Thus, the analytical results need to be validated by further experiments. Nevertheless, it is certain that using local dependence analysis to guide subsequent material research is a feasible and meaningful idea.

4. Conclusions

The goal of this work was to obtain a HEN coating with both high hardness and toughness and to explore the relationships between composition and properties based on data-driven analysis. Through machine learning and multi-objective optimization, a high-entropy nitride coating with an FCC structure, hardness of 33.4 GPa, modulus of 287.7 GPa, and high toughness was designed and prepared in a new HEN system (AlCrSiTiMoTa)N. This work demonstrated an efficient and feasible strategy to design a material with desired yet contradictory properties. Through partial dependence heatmaps, a further study of interpreting optimization results and exploring unknown mapping relationships between elements and mechanical properties of (AlCrSiTiMoTa)N was given, which provides good guidance for the design and research of other HEN in the future.

Declaration of competing interest

The authors declare that they have no known competing financial interests or personal relationships that could have appeared to influence the work reported in this paper.

Acknowledgments

The authors acknowledge the financial support from the National Natural Science Foundation of China (Nos. U21A2044 and 51922002), and the Science Center for Gas Turbine Project (No. P2022-B-IV-008-001), and the Science and Technology Innovation Program of the Hunan Province (2022RC4039).

References

[1] B. Abdallah, M. Kakhia, W. Alsadat, Deposition of TiN and TiAlVN thin films by DC magnetron sputtering, IJSI 11 (2019) 819–831, https://doi.org/10.1108/IJSI-10-2019-0105.
[2] D. Wang, M. Hu, D. Jiang, Y. Fu, Q. Wang, J. Yang, J. Sun, L. Weng, The improved corrosion resistance of sputtered CrN thin films with Cr-ion bombardment layer by layer, Vacuum 143 (2017) 329–335, https://doi.org/10.1016/j.vacuum.2017.06.040.
[3] IgorS. Batraev, VladimirYu Ulianitsky, AlexandrA. Shtertser, DinaV. Dudina, ArinaV. Ukhina, Detonation spraying of binder-free tungsten carbide: in-situ formation of composite coatings, J. Therm. Spray Technol. (2022), https://doi.org/10.1007/s11666-022-01486-x.
[4] M.F. Othman, A.R. Bushroa, W.N.R. Abdullah, Evaluation techniques and improvements of adhesion strength for TiN coating in tool applications: a review, J. Adhes. Sci. Technol. 29 (2015) 569–591, https://doi.org/10.1080/01694243.2014.997379.
[5] R. Hahn, M. Bartosik, R. Soler, C. Kirchlechner, G. Dehm, P.H. Mayrhofer, Superlattice effect for enhanced fracture toughness of hard coatings, Scripta Mater. 124 (2016) 67–70, https://doi.org/10.1016/j.scriptamat.2016.06.030.
[6] X. Xu, X. Wang, S. Wu, L. Yan, T. Guo, K. Gao, X. Pang, A.A. Volinsky, Design of super-hard high-entropy ceramics coatings via machine learning, Ceram. Int. 48 (2022) 32064–32072, https://doi.org/10.1016/j.ceramint.2022.07.145.
[7] E.P. George, D. Raabe, R.O. Ritchie, High-entropy alloys, Nat. Rev. Mater. 4 (2019) 515–534, https://doi.org/10.1038/s41578-019-0121-4.
[8] Y. Wu, C. Xu, J. Guo, Q. Su, G. Du, J. Zhang, Enhanced electrochemical performance by wrapping graphene on carbon nanotube/sulfur composites for rechargeable lithium–sulfur batteries, Mater. Lett. 137 (2014) 277–280, https://doi.org/10.1016/j.matlet.2014.09.044.
[9] Y. Yu, J. Wang, J. Li, H. Kou, H. Duan, J. Li, W. Liu, Tribological behavior of AlCoCrCuFeNi and AlCoCrFeNiTi0.5 high entropy alloys under hydrogen peroxide solution against different counterparts, Tribol. Int. 92 (2015) 203–210, https://doi.org/10.1016/j.triboint.2015.06.013.
[10] B. Gludovatz, A. Hohenwarter, D. Catoor, E.H. Chang, E.P. George, R.O. Ritchie, A fracture-resistant high-entropy alloy for cryogenic applications, Science 345 (2014) 1153–1158, https://doi.org/10.1126/science.1254581.
[11] H. Zhang, H. Fu, X. He, C. Wang, L. Jiang, L.-Q. Chen, J. Xie, Dramatically enhanced combination of ultimate tensile strength and electric conductivity of alloys via machine learning screening, Acta Mater. 200 (2020) 803–810, https://doi.org/10.1016/j.actamat.2020.09.068.
[12] J. He, X. Su, C. Wang, J. Li, Y. Hou, Z. Li, C. Liu, D. Xue, J. Cao, Y. Su, L. Qiao, T. Lookman, Y. Bai, Machine learning assisted predictions of multi-component phase diagrams and fine boundary information, Acta Mater. (2022), 118341, https://doi.org/10.1016/j.actamat.2022.118341.
[13] X. Duan, Z. Fang, T. Yang, C. Guo, Z. Han, D. Sarker, X. Hou, E. Wang, Maximizing the mechanical performance of Ti3AlC2-based MAX phases with aid of machine learning, J. Adv. Ceram. 11 (2022) 1307–1318, https://doi.org/10.1007/s40145-022-0612-4.
[14] C. Guo, X. Duan, Z. Fang, Y. Zhao, T. Yang, E. Wang, X. Hou, A new strategy for long-term complex oxidation of MAX phases: database generation and oxidation kinetic model establishment with aid of machine learning, Acta Mater. 241 (2022), 118378, https://doi.org/10.1016/j.actamat.2022.118378.
[15] C. Guo, J. Shi, F. Ru, C. Zhao, E. Wang, T. Yang, X. Hou, Investigation of multistage oxidation behavior of Al4SiC4 powders with aid of back propagation artificial neural network, Steel Res. Int. (2023), 2200694, https://doi.org/10.1002/srin.202200694.
[16] X. Li, G. Shan, J. Zhang, C.-H. Shek, Accelerated design for magnetic high entropy alloys using data-driven multi-objective optimization, J. Mater. Chem. C 10 (2022) 17291–17302, https://doi.org/10.1039/D2TC03922B.
[17] D. Khatamsaz, B. Vela, P. Singh, D.D. Johnson, D. Allaire, R. Arróyave, Multi-objective materials bayesian optimization with active learning of design constraints: design of ductile refractory multi-principal-element alloys, Acta Mater. 236 (2022), 118133, https://doi.org/10.1016/j.actamat.2022.118133.
[18] X. Chen, S. Lu, X. Wan, Q. Chen, Q. Zhou, J. Wang, Accurate property prediction with interpretable machine learning model for small datasets via transformed atom vector, Phys. Rev. Mater. 6 (2022), 123803, https://doi.org/10.1103/PhysRevMaterials.6.123803.
[19] A. Vellido, The importance of interpretability and visualization in machine learning for applications in medicine and health care, Neural Comput. Appl. 32 (2020) 18069–18083, https://doi.org/10.1007/s00521-019-04051-w.

[20] Y. Iwasaki, R. Sawada, V. Stanev, M. Ishida, A. Kirihara, Y. Omori, H. Someya, I. Takeuchi, E. Saitoh, S. Yorozu, Identification of advanced spin-driven thermoelectric materials via interpretable machine learning, npj Comput. Mater. 5 (2019) 1–6, https://doi.org/10.1038/s41524-019-0241-9.

[21] L. Fang, L. Cheng, J.A. Glerum, J. Bennett, J. Cao, G.J. Wagner, Data-driven analysis of process, structure, and properties of additively manufactured Inconel 718 thin walls, npj Comput. Mater. 8 (2022) 1–15, https://doi.org/10.1038/s41524-022-00808-5.

[22] X. Chen, Y. Du, Y.-W. Chung, Commentary on using H/E and H/E as proxies for fracture toughness of hard coatings, Thin Solid Films 688 (2019), 137265, https://doi.org/10.1016/j.tsf.2019.04.040.

[23] J.-W. Yeh, S.-K. Chen, S.-J. Lin, J.-Y. Gan, T.-S. Chin, T.-T. Shun, C.-H. Tsau, S.-Y. Chang, Nanostructured high-entropy alloys with multiple principal elements: novel alloy design concepts and outcomes, Adv. Eng. Mater. 6 (2004) 299–303, https://doi.org/10.1002/adem.200300567.

[24] J.H. Friedman, L. He, J. Zhang, Z. Li, N. Lin, B. Liu, S. Zhao, K. Jin, H. Chen, H. Yan, F. Peng, Y. Ma, Z. Wu, Greedy function approximation: a gradient boosting machine, Ann. Stat. 29 (2001) 1189–1232, https://doi.org/10.1214/aos/1013203451.

[25] O. Nakonechna, T. Cselle, M. Morstein, A. Karimi, On the behaviour of indentation fracture in TiAlSiN hard thin films, Thin Solid Films (2004) 447–448, https://doi.org/10.1016/S0040-6090(03)01072-1, 406–412.

[26] S. Veprek, H.-D. Männling, M. Jilek, P. Holubar, Avoiding the high-temperature decomposition and softening of (Al1−xTix)N coatings by the formation of stable superhard nc-(Al1−xTix)N/a-Si3N4 nanocomposite, Mat. Sci. Eng. A-Struct. 366 (2004) 202–205, https://doi.org/10.1016/j.msea.2003.08.052.

[27] S. Veprek, A. Niederhofer, K. Moto, T. Bolom, H.-D. Männling, P. Nesladek, G. Dollinger, A. Bergmaier, Composition, nanostructure and origin of the ultrahardness in nc-TiN/a-Si3N4/a- and nc-TiSi2 nanocomposites with HV=80 to ≥105 GPa, Surf. Coating. Technol. 133–134 (2000) 152–159, https://doi.org/10.1016/S0257-8972(00)00957-9.

[28] S. Carvalho, L. Rebouta, E. Ribeiro, F. Vaz, C.J. Tavares, E. Alves, N.P. Barradas, J.P. Riviere, Structural evolution of Ti–Al–Si–N nanocomposite coatings, Vacuum 83 (2009) 1206–1212, https://doi.org/10.1016/j.vacuum.2009.03.009.

[29] W.C. Oliver, G.M. Pharr, An improved technique for determining hardness and elastic modulus using load and displacement sensing indentation experiments, J. Mater. Res. 7 (1992) 1564–1583, https://doi.org/10.1557/JMR.1992.1564.